ON THE NATURE OF THE SOLAR WIND FROM CORONAL PSEUDOSTREAMERS

Y.-M. WANG[1], R. GRAPPIN[2,3], E. ROBBRECHT[4], AND N. R. SHEELEY, JR.[1]

[1] Space Science Division, Naval Research Laboratory, Washington, DC 20375-5352, USA; yi.wang@nrl.navy.mil, neil.sheeley@nrl.navy.mil
[2] LUTH, Observatoire de Paris, CNRS, Université Paris-Diderot, 92195 Meudon, France; roland.grappin@obspm.fr
[3] LPP, Ecole Polytechnique, CNRS, 91128 Palaiseau Cedex, France
[4] Royal Observatory of Belgium, 1180 Brussels, Belgium; eva.robbrecht@oma.be

ABSTRACT

Coronal pseudostreamers, which separate like-polarity coronal holes, do not have current sheet extensions, unlike the familiar helmet streamers that separate opposite-polarity holes. Both types of streamers taper into narrow plasma sheets that are maintained by continual interchange reconnection with the adjacent open magnetic field lines. White-light observations show that pseudostreamers do not emit plasma blobs; this important difference from helmet streamers is due to the convergence of like-polarity field lines above the X-point, which prevents the underlying loops from expanding outward and pinching off. The main component of the pseudostreamer wind has the form of steady outflow along the open field lines rooted just inside the boundaries of the adjacent coronal holes. These flux tubes are characterized by very rapid expansion below the X-point, followed by reconvergence at greater heights. Analysis of an idealized pseudostreamer configuration shows that, as the separation between the underlying holes increases, the X-point rises and the expansion factor f_{ss} at the source surface increases. In situ observations of pseudostreamer crossings indicate wind speeds v ranging from ~350 to ~550 km s^{-1}, with O^{7+}/O^{6+} ratios that are enhanced compared with those in high-speed streams but substantially lower than in the slow solar wind. Hydrodynamic energy-balance models show that the empirical v–f_{ss} relation overestimates the wind speeds from nonmonotonically expanding flux tubes, particularly when the X-point is located at low heights and f_{ss} is small. We conclude that pseudostreamers produce a "hybrid" type of outflow that is intermediate between classical slow and fast solar wind.

Key words: interplanetary medium – solar wind – Sun: corona – Sun: heliosphere – Sun: magnetic topology

1. INTRODUCTION

It is now widely recognized that there are two fundamentally different kinds of coronal streamers: those that separate coronal holes of opposite magnetic polarity, which we refer to here as "helmet streamers"; and those that separate holes of the same polarity, which we call "pseudostreamers" because of the absence of an associated polarity reversal or current sheet in the outer corona (see, e.g., Eselevich et al. 1999; Zhao & Webb 2003; Liu & Hayashi 2006; Liu 2007; Wang et al. 2007a, 2007b; Luhmann et al. 2009; Morgan & Habbal 2010; Morgan 2011; Pasachoff et al. 2011; Riley et al. 2011; Yang et al. 2011). Helmet streamers overlie single (or an odd number of) photospheric neutral lines or loop arcade systems, whereas pseudostreamers overlie two (or an even number of) neutral lines/loop arcades. Both types of streamers taper into narrow plasma sheets that dominate the white-light emission of the outer K corona. The cusp or X-point of a pseudostreamer is usually located well inside heliocentric distance $r \sim 2\,R_\odot$, whereas the cusp/Y-point of a helmet streamer generally lies between 2 and $4\,R_\odot$ and coincides with the inner edge of the heliospheric current sheet (HCS).

While the association between helmet streamers and low-speed wind is well established, there remains considerable uncertainty about the nature of the outflows in the vicinity of pseudostreamers. In Wang et al. (2007a), we noted that the plasma sheets of both pseudostreamers and helmet streamers, as observed in the white-light corona, are composed of fine raylike structures, which we suggested were formed by interchange reconnection at the streamer cusp; thus the plasma sheets in both cases represent material that is continually being released from the underlying closed-field regions (see also Wang et al. 1998, 2000). Interchange reconnection, which involves an exchange of footpoints between open and closed field lines without the creation of any new open flux, has been invoked as a mechanism for maintaining the quasirigid rotation of coronal holes (e.g., Nash et al. 1988; Wang et al. 1989, 1996; Wang & Sheeley 1993, 2004; Fisk et al. 1999; Lionello et al. 2005; Raju et al. 2005; Kahler et al. 2010; Krista et al. 2011), for regulating the strength of the heliospheric magnetic field (Crooker et al. 2002; Owens & Crooker 2006; Schwadron et al. 2010; Crooker & Owens 2011), and for generating slow solar wind from closed-field regions (Schwadron et al. 1999; Antiochos et al. 2011; Edmondson 2011).

In addition to the outflow occurring in the plasma sheet itself, material also escapes continually along the open field lines rooted just inside the boundaries of the adjacent coronal holes (whether their polarities are the same or not). In the case of pseudostreamers, we have previously postulated that these flows would have high asymptotic speeds v (Wang et al. 2007b), on the supposition that the reconvergence of the field lines above the X-point would result in small values of the expansion factor f_{ss} (Sheeley & Wang 1991), which is empirically found to be inversely correlated with v (see, e.g., Wang & Sheeley 1990; Arge & Pizzo 2000; Poduval & Zhao 2004). In the framework of the potential-field source-surface (PFSS) model, f_{ss} is defined as the factor by which a given flux tube expands in solid angle between $r = R_\odot$ and the source surface $r = R_{ss}$, where the coronal field is assumed to become radial. In terms of the field strengths at the footpoint of the flux tube and at the source surface,

$$f_{ss} = \left(\frac{R_\odot}{R_{ss}}\right)^2 \frac{B_0}{B_{ss}}, \qquad (1)$$

where we henceforth set $R_{ss} = 2.5\,R_\odot$, which gives a reasonable match to the observed locations and sizes of He I 1083.0 nm

coronal holes throughout the solar cycle (see Figure 2 in Wang et al. 1996). In fact, as we demonstrate in Section 4, the pseudostreamer topology is characterized by a wide range of expansion factors; unless the cusp is located at very low heights, the rapid expansion that occurs below the X-point dominates over the subsequent reconvergence of field lines, leading to relatively large values of f_{ss} and, by implication, relatively low wind speeds.

Boundaries between wind streams of the same polarity, presumably corresponding to in situ pseudostreamer crossings, have been identified in a number of studies (Neugebauer et al. 2002, 2004; Liewer et al. 2004; Wang et al. 2010). At these non-HCS stream interfaces, the wind-speed profiles generally show a pronounced dip, although the minimum velocities ($\sim$350–550 km s^{-1}) tend to be higher than those encountered at HCS crossings. The proton densities are enhanced, but less so than at sector boundaries. In some cases, narrow density spikes are present in the hourly averaged data, which are either remnants of the pseudostreamer plasma sheet or the result of compressional interactions between the neighboring streams (Wang et al. 2010). It should be noted that, in the examples identified so far, the like-polarity holes tend to be located on one side of and well away from the ecliptic plane, so that the spacecraft undergoes only a peripheral encounter with the pseudostreamer, rather than sampling the region directly in between the two holes. The largest and longest-lived pseudostreamers are centered at midlatitudes between the polar holes and lower-latitude holes in the same hemisphere; unfortunately, their plasma sheet extensions are oriented perpendicular to the Sun's rotation axis, preventing an unambiguous periodic sampling by the *Ulysses* spacecraft.

According to the recently proposed "S-web" model (Antiochos et al. 2011; Linker et al. 2011), the bulk of the slow solar wind originates via interchange reconnection from a network of separatrices and quasi-separatrix layers, which surround the HCS, and which are associated with very narrow open-field corridors that are conjectured to link all of the fragmentary open-field regions within a given unipolar area. However, ultra-fine-meshed numerical computations and topological analysis by Titov et al. (2011) show that most of the postulated connecting corridors have zero width at the photosphere, and that the linking or merging of like-polarity holes tends to occur at greater heights, as their boundaries fan out into the corona. (This merging with height is an obvious and long-recognized implication of the PFSS model, where all of the flux is required to be open at the source surface.) The most prominent separatrices present in the outer corona are those associated with pseudostreamers and the HCS, with the network of pseudostreamer plasma sheets branching off from the HCS (compare Figures 7–10 in Wang et al. 2007b with Figure 7(a) in Antiochos et al. 2011 or Figure 10 in Titov et al. 2011). In addition, however, the heliospheric S-web is criss-crossed by finer-scale structure that arises from the presence of small bipoles and mixed-polarity flux within the underlying coronal holes. This fine structure presumably corresponds observationally to coronal plumes; indeed, we have previously remarked on the similar magnetic topologies of plumes and pseudostreamers, with the latter effectively representing "giant plumes" (Wang et al. 2007a; Wang & Muglach 2008).

As Antiochos et al. (2011) themselves remark, the S-web is not space filling, but is permeated by the outflows from the embedded coronal holes. Thus, only a fraction of the low-latitude wind (which is associated with the HCS, pseudostreamer plasma

sheets, and plumes) results from interchange reconnection. Moreover, it has yet to be demonstrated that interchange reconnection necessarily gives rise to low wind speeds, or that the wind plasma will have the compositional properties of closed coronal loops, an assumption that is one of the main motivations for such slow wind models (see Schwadron et al. 1999; Feldman et al. 2005; Zhao et al. 2009).

It is also worth pointing out that the high-resolution photospheric magnetic map employed by Antiochos et al. (2011) and Titov et al. (2011) to derive the global distribution of separatrices and quasi-separatrix layers does not adequately represent the polar regions, which have been artificially smoothed because the line-of-sight field is poorly observed near the limb. In reality, of course, small bipoles emerge everywhere on the solar surface, including near the poles (as is evident from a cursory glance at any high-resolution EUV image), and the high-latitude fields have far more fine structure than indicated by Figure 5 of Antiochos et al. (2011) or Figure 9 of Titov et al. (2011). Thus, the fine-scale structure in the low-latitude S-web derived by these authors must in fact extend toward the poles, where *Ulysses* has demonstrated that the solar wind is almost uniformly fast near sunspot minimum. Indeed, the well-known difficulty in detecting in situ signatures of polar plumes argues against the fine structure of the S-web being a major source of slow solar wind.

Our objective here is to clarify some of the questions raised above about the nature of the solar wind from pseudostreamers. We first discuss attempts to identify outflows in and around pseudostreamers using white-light coronal observations (Section 2). Section 3 focuses on in situ observations of pseudostreamer crossings. Section 4 discusses the relationship between the height of the X-point and the expansion factor, while Section 5 presents hydrodynamic energy-balance computations supporting the conclusion that pseudostreamers produce relatively slow wind, provided that the X-point is located well above the solar surface. Our results are summarized and their implications discussed in Section 6.

2. THE QUIESCENT NATURE OF WHITE-LIGHT PSEUDOSTREAMERS

In instantaneous images of the white-light corona, the plasma sheet extensions of pseudostreamers are barely distinguishable from those of ordinary helmet streamers, both appearing as bright, narrow stalks when seen edge-on in the sky plane but as fainter, fanlike structures when viewed face-on. The main difference is that the pseudostreamer plasma sheets start at much lower heights than their counterparts with polarity reversals, with their cusps often only seen in eclipse pictures (or in EUV images whose fields of view extend well above the solar limb).

Figure 1 shows an edge-on pseudostreamer plasma sheet above the southwest limb on 2007 April 26, as observed with the Large Angle and Spectrometric Coronagraph (LASCO) C2 coronagraph on the *Solar and Heliospheric Observatory* (*SOHO*). The background-subtracted image in the top panel, with field of view $r \sim$ 2–6 $R_\odot$, was recorded at 19:27 UT; a bright helmet streamer may also be seen above the northwest limb. (PFSS extrapolations indicate that the helmet streamer lies between the negative-polarity north polar hole and an elongated positive-polarity hole in the southern hemisphere, while the pseudostreamer is located between the latter hole and the positive-polarity south polar hole.) The bottom panel shows the result of subtracting the 19:27 UT image from
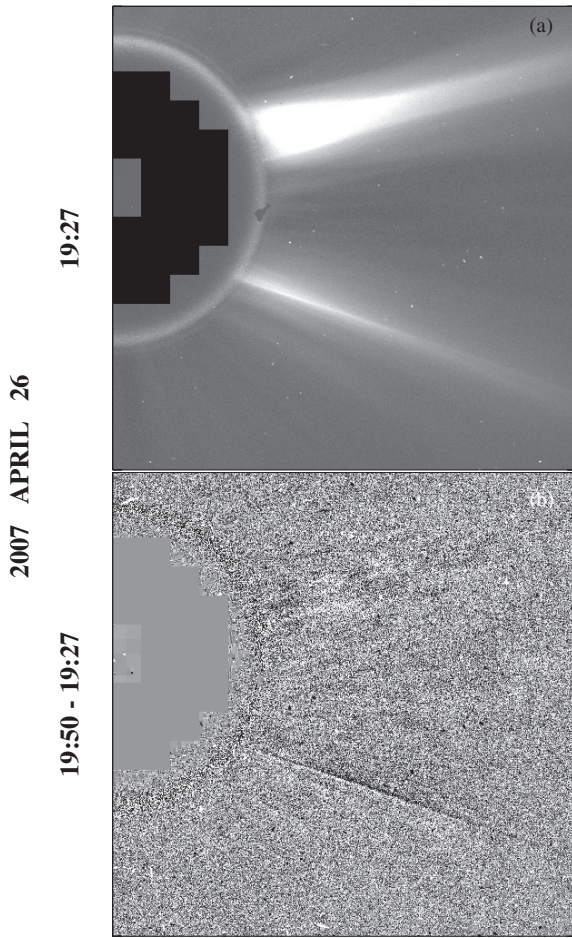
Figure 1. Edge-on plasma sheet extension ("stalk") of a pseudostreamer observed above the southwest limb on 2007 April 26 with the LASCO C2 coronagraph. A helmet streamer is also present above the northwest limb. (a) Image recorded at 19:27 UT, with a monthly minimum background subtracted. (b) Difference of images recorded at 19:50 and 19:27 UT; white (black) indicates an increase (decrease) in the local brightness at the later time. Occulting disk extends out to $r \sim 2\ R_{\odot}$. The helmet streamer is immediately recognizable as such from the fact that its cusp is located in the middle of the 2–6 $R_{\odot}$ field of view, in contrast to that of the pseudostreamer, which lies hidden under the occulter.

one taken at 19:50 UT; here, as it rotates past the sky plane and moves to higher apparent latitudes, the pseudostreamer stalk appears as a linear structure with white (black) on its poleward (equatorward) side. In contrast to this purely transverse motion, outward-moving inhomogeneities ("blobs") with white leading black are visible around the helmet streamer in the northern hemisphere.

After constructing running-difference movies from LASCO C2 and C3 images recorded during 2007 April 26–27 and extracting radially oriented strips centered on the average position angle (P.A.) of the pseudostreamer (P.A. $\sim 242°$), we assembled the distance–time map displayed in the top panel of Figure 2. For comparison, we also display a map centered on the helmet streamer at P.A. $\sim 287°$ (bottom panel). What is striking is the absence of any prominent tracks in the r–t map for the pseudostreamer. Very faint slanted patterns may be discerned during April 26; although we earlier interpreted such faint tracks, with slopes on the order of the sound speed, as evidence for relatively fast outflows from pseudostreamers (see Figure 11(a) in Wang et al. 2007b, and the accompanying discussion), an alternative interpretation is that they simply

represent background/foreground material in the line of sight. In contrast, the r–t map for the helmet streamer unambiguously shows a series of long, curved tracks that extend through the C3 field of view and are a characteristic signature of gradually accelerating streamer blobs (Sheeley et al. 1997; Wang et al. 1998, 2000; Jones & Davila 2009; Song et al. 2009).

This failure to detect plasma blobs from pseudostreamers, employing either *SOHO*/LASCO or *STEREO*/SECCHI white-light observations, is understandable when one considers the magnetic topology of a pseudostreamer. Above the cusp/X-point, the like-polarity field lines from the two neighboring coronal holes converge; the field there thus becomes strong enough to confine the underlying loops. In helmet streamers, on the other hand, the field strength goes to zero where the opposite-polarity field lines meet above the cusp, allowing the underlying arcade loops to expand outward (see, e.g., Suess et al. 1996; Einaudi et al. 2001; Endeve et al. 2004; Chen et al. 2009). These loops then reconnect with each other and pinch off to form flux ropes (as depicted in Figure 8(b) of Wang et al. 2000), which are observed as blobs and V-shaped features if their axes are perpendicular to the sky plane, but as larger arch-like structures if their axes lie in the sky plane (Sheeley et al. 2009). The pinching-off of the expanding helmet-streamer loops does not require the presence of open flux (i.e., the blobs are not formed by interchange reconnection), but the blobs/flux ropes may subsequently undergo interchange reconnection with open field lines and partially or fully detach from their anchor points at the Sun (see Gosling et al. 1995; Wang et al. 1998; Crooker et al. 2002, 2004; Owens & Crooker 2006; Crooker & Owens 2011; Rouillard et al. 2011).

3. PSEUDOSTREAMER CROSSINGS AT 1 AU

Wind stream interfaces without polarity reversals, which may coincide with pseudostreamer crossings at 1 AU, have been described in a number of earlier investigations. We begin here by reviewing the case of Carrington rotation (CR) 1953 (starting date 1999 August 18), which was also discussed by Neugebauer et al. (2002, 2004) and Liewer et al. (2004).

The latitude–longitude maps in Figure 3 display, for CR 1953, the distribution of He I 1083.0 nm intensity observed by the National Solar Observatory (NSO/Kitt Peak), with white areas representing coronal holes (top panel), the footpoints of open field lines derived from a PFSS extrapolation of NSO magnetograph measurements (middle panel), and the source-surface field (bottom panel). The derived coronal holes are color-coded according to the local values of the expansion factor $f_{\rm ss}$, and have positive (negative) polarity if the background area is light gray (dark gray). Colored diamonds indicate the predicted wind speeds (or values of $f_{\rm ss}$) in the ecliptic plane, with white lines connecting the Earth-directed flux tubes to their photospheric footpoints. (The conversion between $f_{\rm ss}$ and v is the same as that used in Figure 1 of Wang et al. (2010), which compares the expansion factors with the observed near-Earth wind speeds over the entire period 1976–2009.) Longitudinal intervals where flux tubes from like-polarity holes meet in the ecliptic, corresponding to predicted pseudostreamer crossings, are enclosed in boxes.

Figure 4 (top panel) displays the corresponding *ACE* measurements of wind speed v, proton density $n_{\rm p}$, and oxygen charge-state ratio $n_{\rm O^{7+}}/n_{\rm O^{6+}}$; the bottom panel gives the spiral angle of the interplanetary magnetic field (IMF) and the abundance ratio $n_{\rm Fe}/n_{\rm O}$, which is considered to be a measure of the relative enrichment in elements of low first-ionization potential (FIP; see,
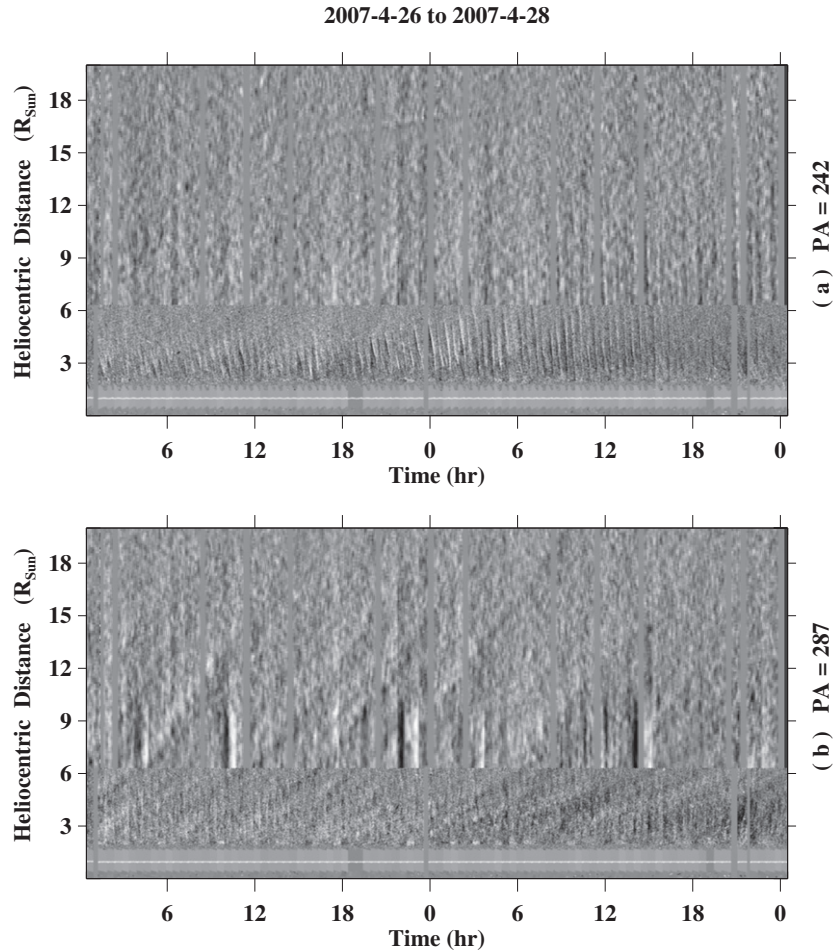
2007-4-26 to 2007-4-28

Figure 2. Height–time maps showing the outflows during 2007 April 26–27 (a) above the pseudostreamer at P.A. $\sim 242°$ in Figure 1 and (b) above the helmet streamer at P.A. $\sim 287°$ in Figure 1. The maps were constructed from LASCO C2 and C3 running-difference images, by excising from each image a radial strip centered on the streamer axis and arranging the strips in a time-ordered sequence. Streamer blobs, characterized by a series of upward curving tracks, are clearly visible only above the helmet streamer.

e.g., Geiss et al. 1995; von Steiger et al. 2000). The data are plotted in time-reversed Carrington format, and have been shifted by an average Sun–Earth transit time of 4 days to bring them into approximate phase with the Carrington maps of Figure 3. The vertical dashed lines mark the stream–stream interfaces without polarity reversals that lie within the boxed longitude ranges in Figure 3 and are assumed to represent pseudostreamer crossings at 1 AU.

As indicated by the blue diamonds inside the two boxed areas of Figure 3, the expansion factor model predicts large values of f_{ss} ($\gtrsim 20$) and hence relatively low wind speeds ($\lesssim 450$ km s^{-1}) at both pseudostreamer crossings. From Figure 4, we see that the observed minimum velocities at the corresponding stream interfaces are $v \sim 390$ km s^{-1} (at longitude $\phi \sim 121°$) and $v \sim 480$ km s^{-1} (at $\phi \sim 306°$), in qualitative agreement with the expansion factor model. As noted by Neugebauer et al. (2002, 2004) and Liewer et al. (2004), the wind speeds are higher than those typically measured at HCS crossings (where the average value is ~ 365 km s^{-1} according to Figure 7 of Borrini et al. 1981), while the proton densities are lower. The oxygen charge-state ratios $n_{O^{7+}}/n_{O^{6+}}$ in the vicinity of the pseudostreamers have values of order 0.1; as may be seen from Table 2 in Wang et al. (2009) or Table 2 in Zhao et al. (2009), these values are smaller than those typically found in low-speed wind (where $n_{O^{7+}}/n_{O^{6+}} \gtrsim 0.2$), but larger than those encountered in high-speed streams (where $n_{O^{7+}}/n_{O^{6+}} \lesssim 0.05$). The Fe/O ratios at the

two pseudostreamer crossings are ~ 0.10 ($\phi \sim 121°$) and ~ 0.07 ($\phi \sim 306°$); for comparison, Table 2 in Wang et al. (2009) shows n_{Fe}/n_O to have characteristic values $\gtrsim 0.10$ in slow wind ($v \lesssim 450$ km s^{-1}) and $\lesssim 0.07$ in fast wind ($v \gtrsim 550$ km s^{-1}). Unlike in the cases presented in Wang et al. (2010), here we do not see prominent density spikes that might represent either remnant pseudostreamer plasma sheets or compressional structures, where these abundance ratios are sometimes more strongly enhanced.

The pseudostreamer crossings in Figures 3 and 4 occurred at sunspot maximum, when coronal mass ejection events are frequent and the solar wind originates from a motley collection of small coronal holes scattered over a wide range of latitudes. We now consider an example from the recent solar minimum. Figure 5 shows, for CR 2070 (starting date 2008 May 13), the distribution of Fe XII 19.5 nm emission observed by *STEREO*/EUVI A (top panel), the open-field regions derived from a PFSS extrapolation of photospheric magnetic measurements from the Mount Wilson Observatory (MWO; middle panel), and the source-surface field (bottom panel). Inside the boxed area, field lines from two separate segments of the equatorward extension of the south polar hole meet in the ecliptic plane. The blue and green diamonds around the point of intersection indicate an average wind speed of order 450 km s^{-1}.

Figure 6 shows the corresponding *ACE* observations for CR 2070, again plotted in time-reversed order and shifted by

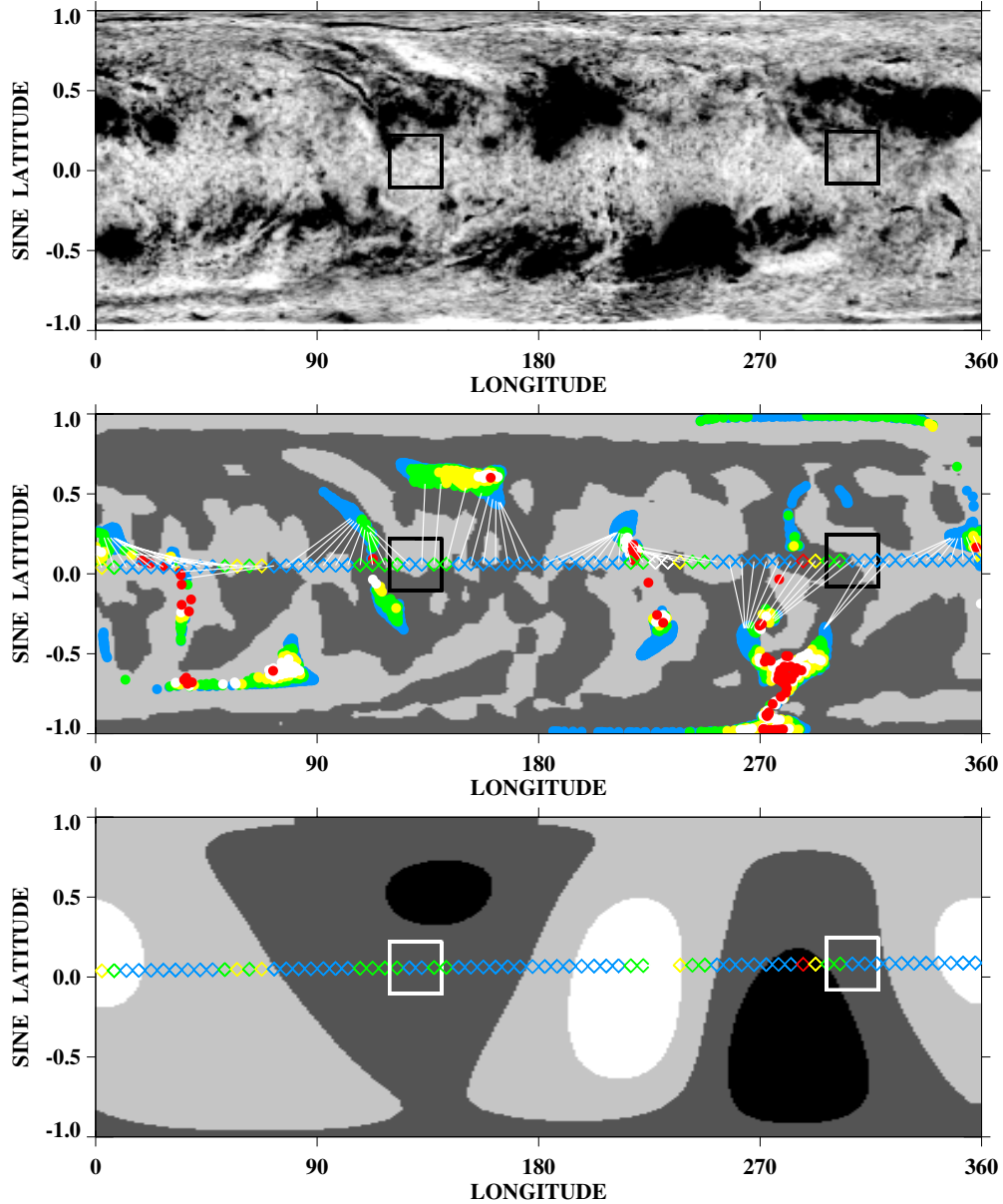## CARRINGTON ROTATION 1953 (NSO)

Figure 3. Latitude–longitude maps showing the probable locations (boxed areas) of pseudostreamers near the ecliptic plane during CR 1953 (starting date 1999 August 18). Top panel: He I 1083.0 nm map (NSO/Kitt Peak). White areas represent coronal holes or filament channels, dark areas are active regions or filaments. Middle panel: coronal holes derived from a PFSS extrapolation (with $R_{ss} = 2.5\ R_\odot$) of NSO photospheric field measurements. Colored dots represent footpoints of open field lines and are coded according to the associated expansion factors or asymptotic wind speeds. Blue: $v < 450$ km s^{-1} ($f_{ss} > 20$); green: $v = 450$–550 km s^{-1} ($20 > f_{ss} > 10$); yellow: $v = 550$–650 km s^{-1} ($10 > f_{ss} > 7$); white: $v = 650$–750 km s^{-1} ($7 > f_{ss} > 4.5$); red: $v > 750$ km s^{-1} ($f_{ss} < 4.5$). The underlying polarity of the photospheric field is indicated by light gray (if $B_r > 0$) or dark gray (if $B_r < 0$). Colored diamonds show the predicted wind speeds in the ecliptic plane (neglecting the effect of interactions between wind streams), with white lines pointing to the corresponding source regions. Bottom panel: source-surface field B_{ss}, with the colored diamonds again indicating the predicted ecliptic wind speeds. Black: $B_{ss} < -0.2$ G; dark gray: -0.2 G $< B_{ss} < 0$ G; light gray: 0 G $< B_{ss} < +0.2$ G; white: $B_{ss} > +0.2$ G.

4 days to allow for propagation to 1 AU. The vertical dashed line at longitude $\phi \sim 200°$ marks the probable location of the pseudostreamer. There, the wind speed dips to a value of $\sim$460 km s^{-1}, while the proton densities, oxygen freezing-in temperatures, and Fe/O ratios are moderately elevated over their values in the surrounding coronal-hole interiors. In contrast, at the nearby HCS crossing at $\phi \sim 220°$, v falls to values as low as $\sim$340 km s^{-1}, while n_p, $n_{O^{7+}}/n_{O^{6+}}$, and n_{Fe}/n_O are sharply enhanced.

Finally, we consider a pseudostreamer crossing that occurred during the rising phase of the current sunspot cycle. Figure 7

displays the distribution of Fe XII 19.5 nm emission observed by *STEREO*/EUVI B during CR 2104 (starting date 2010 November 26), the open-field regions derived from a PFSS extrapolation of NSO photospheric measurements, and the source-surface field. A pair of negative-polarity holes may be seen near the equator; the hole to the southwest has recently formed following the emergence of the active region along its equatorward edge. As indicated by the yellow and red diamonds inside the boxed area, the predicted ecliptic wind speeds at the boundary between the two holes are high ($\sim$550–775 km s^{-1}). As shown by the *ACE* measurements in Figure 8, the pseudostreamer is
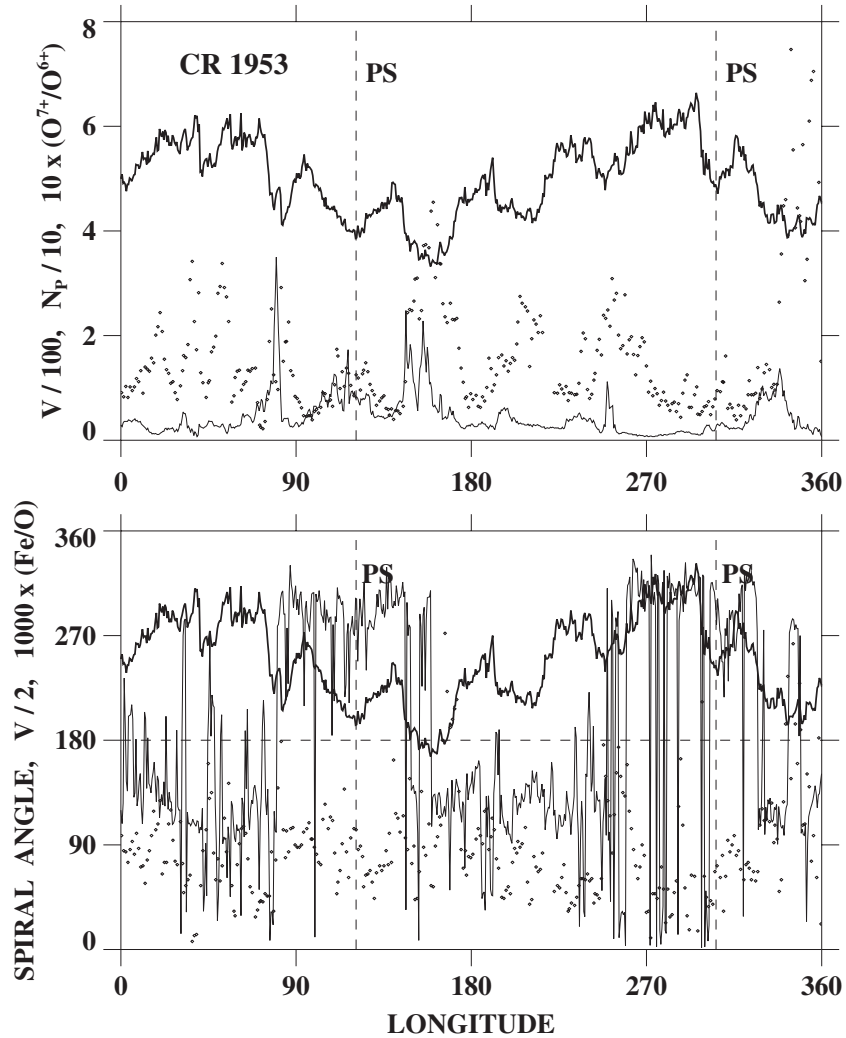
Figure 4. Solar wind measurements by *ACE* during CR 1953, plotted as a function of Carrington longitude (so that time runs from right to left in each panel, as in Figure 3). Top panel: variation of hourly averaged wind speed v in units of 100 km s^{-1} (thick solid line), hourly averaged proton density n_p in units of 10 cm^{-3} (thin solid line), and 2 hr averages of the oxygen charge-state ratio $(n_{O^{7+}}/n_{O^{6+}}) \times 10$ (small diamonds). Vertical dashed lines mark the stream–stream interfaces (previously identified by Neugebauer et al. 2002, 2004 and Liewer et al. 2004) that correspond to the boxed areas in Figure 3 and represent probable pseudostreamer crossings. Bottom panel: variation of the IMF spiral angle in degrees (thin solid line), measured counterclockwise from the Sun–Earth axis and lying in the quadrant 90°–180° (270°–360°) if the flux tube points away from (toward) the Sun. Also plotted is $v/2$ in km s^{-1} (thick solid line) and the abundance ratio $(n_{Fe}/n_O) \times 1000$ (small diamonds). All measurements have been mapped back to the source surface (so as to be in phase with the Carrington maps of Figure 3), assuming a 4 day Sun–Earth propagation time (similar results are obtained if the backward-mapping is done using the observed wind speeds).

located within a single high-speed stream, which has apparently formed through the merging of the outflows from the neighboring coronal holes or their fragmentary pieces. The exact position of the pseudostreamer within the merged stream is difficult to determine, but (as indicated by the vertical dashed line) we have taken it to coincide with the small enhancement in the O^{7+}/O^{6+} ratio near $\phi \sim 159°$. In any case, the expansion factor model overestimates the actual wind speeds in the vicinity of the pseudostreamer, which are on the order of 550 km s^{-1}.

In these examples, any pseudostreamer plasma sheet that may have existed in the corona is no longer identifiable at 1 AU, having apparently been smeared out and mixed with the surrounding flows during the Sun–Earth transit. We are thus unable to characterize the intrinsic properties of the plasma sheet. On the other hand, it appears that the outflows immediately adjacent to the plasma sheet have properties that differ from the "classical" slow solar wind, and which in some ways appear to be intermediate between those of fast and slow wind.

4. DEPENDENCE OF THE EXPANSION FACTOR ON THE HEIGHT OF THE X-POINT

The behavior of open flux at the facing boundaries of like-polarity holes is anomalous in that, instead of expanding monotonically with height, the flux initially expands rapidly but then reconverges as the field lines from the two holes "collide" above the cusp. It is instructive to consider the following illustrative case (see also Sheeley & Wang 1991).

Let the (arbitrarily normalized) photospheric field be represented by a linear superposition of the Legendre polynomials of order 1 and 5:

$$B_r(R_\odot, L) = P_1(\sin L) + k\,P_5(\sin L)$$
$$= \sin L + (k/8)(63\sin^5 L - 70\sin^3 L + 15\sin L),$$
(2)

where L denotes heliographic latitude and $k > 0$ is a constant. With three polarity zones in each hemisphere, $P_5(L)$ modifies

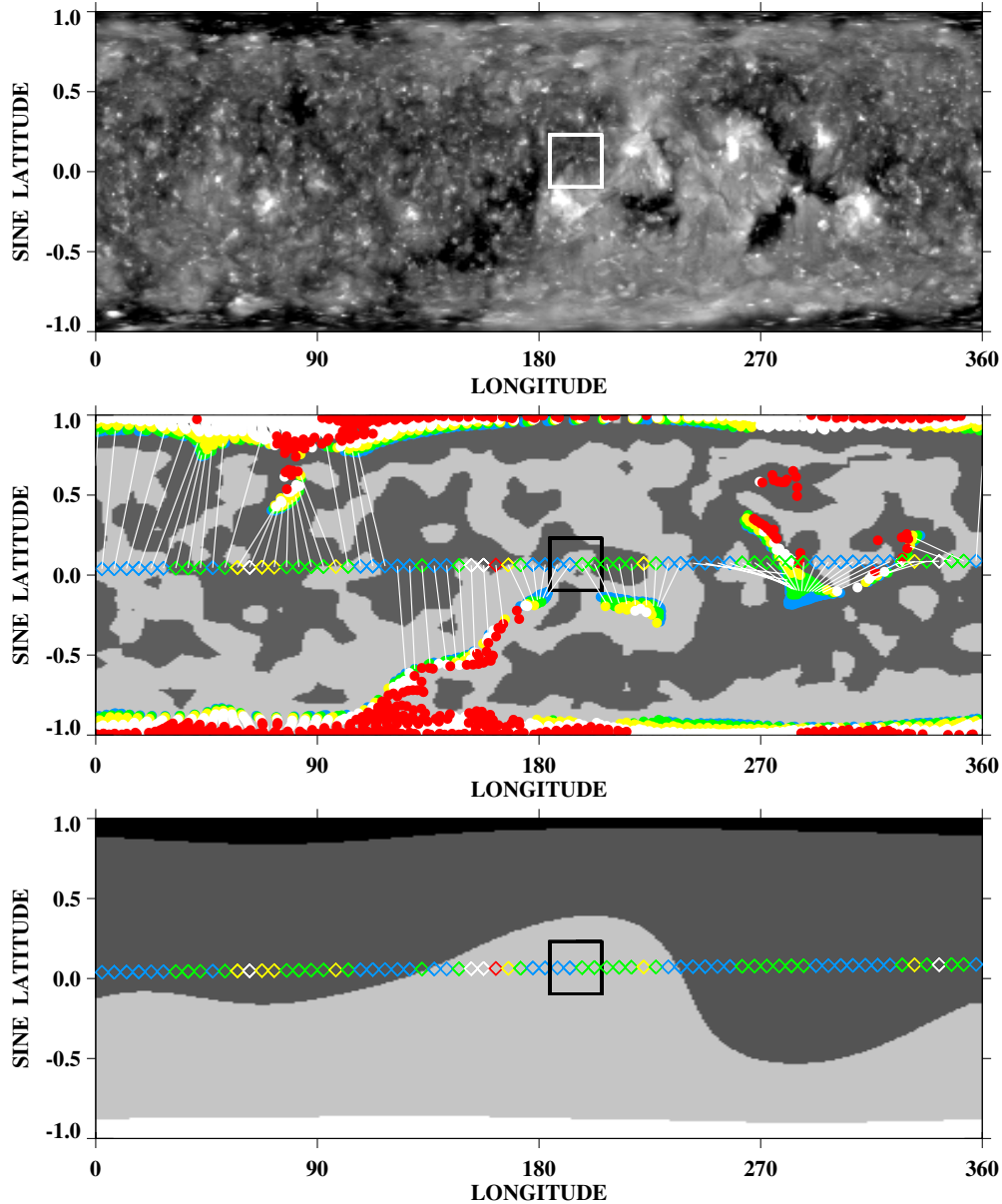## CARRINGTON ROTATION 2070 (MWO)

Figure 5. Latitude–longitude maps for CR 2070 (starting date 2008 May 13), with the boxed area indicating the probable site of a pseudostreamer located between two segments of an equatorward extension of the south polar hole. Top panel: distribution of Fe XII 19.5 nm emission observed by *STEREO*/EUVI A. Middle panel: open-field regions derived by applying a PFSS extrapolation to MWO photospheric measurements. Bottom panel: source-surface field. Symbols as in Figure 3.

the background dipole distribution by introducing a midlatitude band having the opposite sign to the poleward and equatorward zones; the width and strength of this band can be varied by adjusting the parameter k. Setting $k = 3$, 10, 33, and 66 and applying a PFSS extrapolation with $R_{ss} = 2.5 R_{\odot}$ to Equation (2), we obtain the coronal field-line configurations displayed in the left column of Figure 9. In the right column, we plot, for each of these configurations, the latitudinal variation at $r = R_{ss}$ of the expansion factor f_{ss} and of the source-surface field strength $|B_{ss}|$.

The model pseudostreamer with its underlying double arcade is centered above the midlatitude polarity band. As k increases, this band widens, the separation between the like-polarity holes on each side of it increases, and the X-point rises. For very large

k (Figure 9(d)), the X-point reaches the source surface and a hole of the opposite polarity forms within the midlatitude band; at the same time, the pseudostreamer splits into two separate helmet streamers. From the right-hand plots in Figure 9, we see that the values of f_{ss}, including those at the latitudinal location of the streamer, increase as k increases and the X-point rises. We also note that f_{ss} undergoes a discontinuous jump from one side of the pseudostreamer to the other: the flux from the lower-latitude hole is "pushed back" as it encounters the stronger field from the polar hole, so that the expansion factors for this photospheric configuration are smaller on the equatorward side of the pseudostreamer than on the poleward side.

Let us denote by $f(r)$ the factor by which a given flux tube expands in solid angle between the coronal base $r = R_{\odot}$
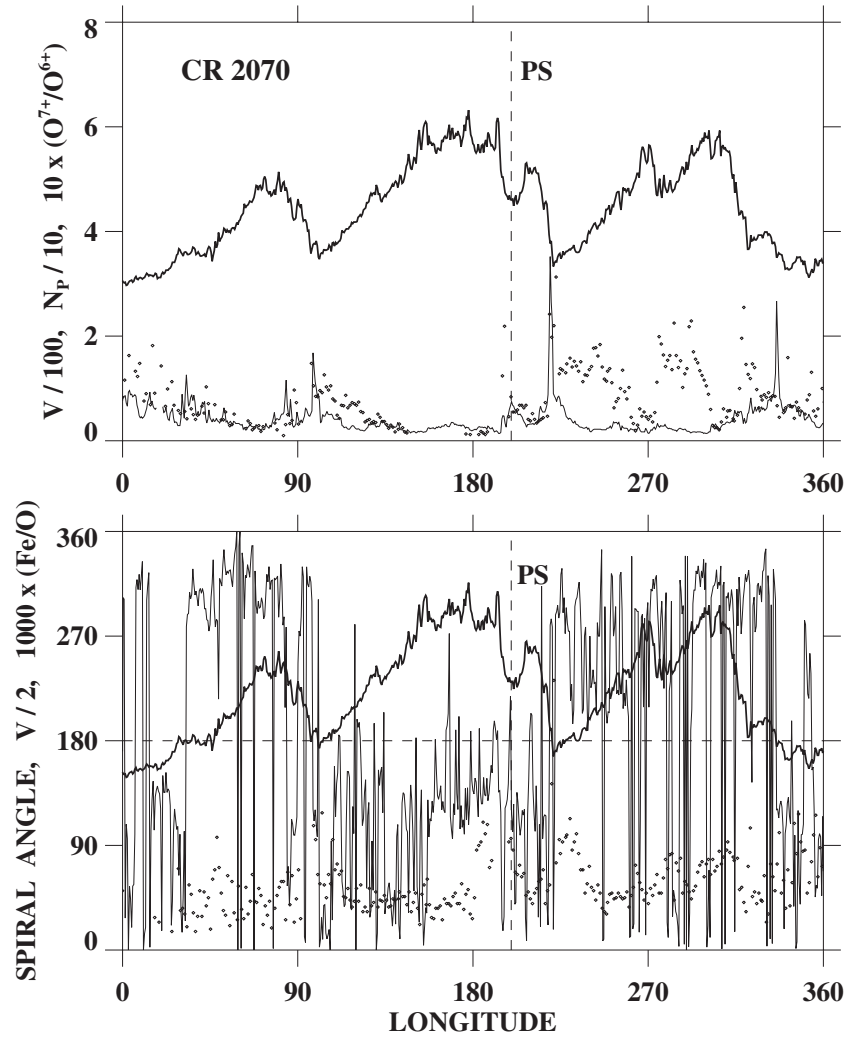
Figure 6. Solar wind measurements by *ACE* during CR 2070, shifted by 4 days to allow for the average Sun–Earth transit time and plotted as a function of Carrington longitude. Vertical dashed line marks the stream–stream interface that corresponds to the boxed area in Figure 5. Top panel: wind speed v in units of 100 km s^{-1} (thick solid line), proton density n_p in units of 10 cm^{-3} (thin solid line), and oxygen charge-state ratio $(n_{O^{7+}}/n_{O^{6+}}) \times 10$ (small diamonds). Bottom panel: spiral angle in degrees (thin solid line), $v/2$ in km s^{-1} (thick solid line), and $(n_{Fe}/n_O) \times 1000$ (small diamonds).

and heliocentric radius r. Figure 10 shows the behavior of $f(r) \propto (r^2 B_r)^{-1}$ for an open flux tube that is rooted on one side of the pseudostreamer and passes close to the X-point; the four curves correspond to setting $k = 3$ ($R_X = 1.11\,R_\odot$), $k = 5$ ($R_X = 1.25\,R_\odot$), $k = 10$ ($R_X = 1.47\,R_\odot$), and $k = 33$ ($R_X = 1.99\,R_\odot$). In all cases, $f(r)$ increases rapidly at low heights, attaining a maximum at $r \sim R_X$; it then falls toward a plateau where $f(r) \simeq f_{ss}$. It may be seen from Figure 10 that f_{ss} exceeds ~ 10 (~ 20) if the X-point is located above $\sim 1.25\,R_\odot$ ($\sim 1.4\,R_\odot$). According to the empirical v–f_{ss} relation, $f_{ss} \gtrsim 10$ ($\gtrsim 20$) corresponds to wind speeds $v \lesssim 550$ km s^{-1} ($\lesssim 450$ km s^{-1}). Conversely, high wind speeds ($v \gtrsim 550$ km s^{-1}) are expected at the pseudostreamer only when $f_{ss} \lesssim 10$ or $R_X \lesssim 1.25\,R_\odot$. As we demonstrate below, however, the v–f_{ss} relation, based implicitly on the assumption of monotonic expansion, significantly overestimates the wind speeds for small values of R_X and f_{ss}.

5. HYDRODYNAMIC SIMULATIONS

The question of what wind speeds are to be expected from pseudostreamers can also be approached via hydrodynamic or

MHD simulations (see, e.g., Lionello et al. 2009; Riley et al. 2010). The results, of course, will depend on what assumptions are made about the coronal heating function (see the review of Cranmer 2009). As demonstrated in Wang et al. (2009), if the heating rate is taken to depend on the local magnetic field strength, rapid flux-tube expansion causes the heating to be concentrated near the coronal base, driving a large mass flux but reducing the energy available per proton; in contrast, if the field diverges slowly, more of the energy is deposited near the sonic point, leading to greater acceleration and higher asymptotic wind speeds (cf. Leer & Holzer 1980). In the "hybrid" case where rapid expansion is followed by reconvergence, we might expect the combination of heating low and high in the corona to produce intermediate speeds.

To investigate the consequences of nonmonotonic expansion, we employ the one-dimensional, single-fluid code described in Pinto et al. (2009), which explicitly includes a chromospheric–coronal transition region and the effects of energy deposition and heat conduction, while allowing for an arbitrary variation of the magnetic field B with r. Acceleration is by the thermal pressure force, with no further momentum addition (e.g., by Alfvén wave pressure) being included. As in
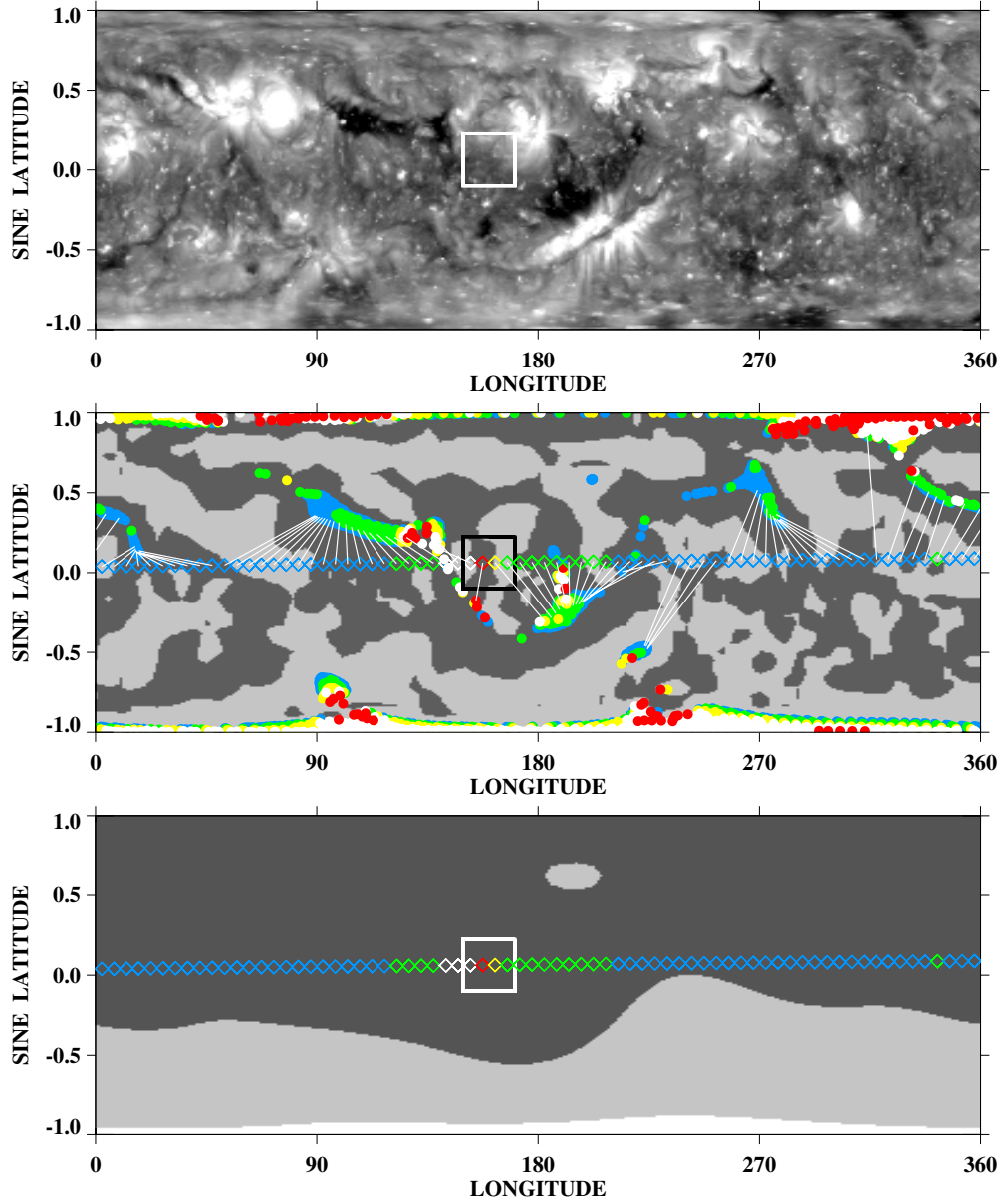
CARRINGTON ROTATION 2104 (NSO)

Figure 7. Latitude–longitude maps for CR 2104 (starting date 2010 November 26), showing the probable site of a pseudostreamer lying between negative-polarity holes near the equator. Top panel: distribution of Fe XII 19.5 nm emission observed by EUVI B. Middle panel: open-field regions derived by applying a PFSS extrapolation to the NSO photospheric map for CR 2104. Bottom panel: source-surface field. Symbols as in Figure 3.

Pinto et al. (2009), we adopt an illustrative heating function with energy flux density given by

$$F_{\rm h}(r) = F_{\rm h0} \left(\frac{B}{B_0} \right)^{\mu}, \qquad (3)$$

where we again take $\mu = 3/2$ and $F_{\rm h0} = 8 \times 10^5$ erg cm^{-2} s^{-1}. To represent an open flux tube at the boundary of a pseudostreamer, we let the magnetic field vary with radius as

$$B(r) = B_0 \left(\frac{R_\odot}{r} \right)^{\nu} \left[\frac{1 + (r/R_{\rm X})^{\nu-1}}{1 + (R_\odot/R_{\rm X})^{\nu-1}} \right] \left[\frac{1 + (R_\odot/R_{\rm ss})}{1 + (r/R_{\rm ss})} \right], \qquad (4)$$

where $R_{\rm ss} = 2.5\, R_\odot$, and where $\nu > 2$ and $R_{\rm X} < R_{\rm ss}$ are adjustable parameters. The field strength thus falls off as $r^{-\nu}$

for $r \lesssim R_{\rm X}$, as r^{-1} for $R_{\rm X} \lesssim r \lesssim 2.5\, R_\odot$, and as r^{-2} for $r \gg 2.5\, R_\odot$.

Solutions are obtained by numerically integrating the equations of mass, momentum, and energy conservation, employing a nonuniform grid extending from $r = R_\odot$ (where $\Delta r = 10^{-4}\, R_\odot$) to $r = 31.5\, R_\odot$ (where $\Delta r = 0.3\, R_\odot$) and imposing nonreflecting boundary conditions at the photosphere (see Pinto et al. 2009; Grappin et al. 1997). Figure 11 shows the radial variation of the flow speed $u(r)$, temperature $T(r)$, density $n(r)$, expansion factor $f(r) = (R_\odot/r)^2 [B_0/B(r)]$, and mechanical energy flux density $F_{\rm h}(r)$ for the cases $\nu = 7$, $R_{\rm X} = 1.1\, R_\odot$ (thick solid lines) and $\nu = 7$, $R_{\rm X} = 1.5\, R_\odot$ (thin solid lines). As expected, the effect of extending the region of rapid ($B \propto r^{-7}$) expansion to greater heights (from 1.1 to 1.5 $R_\odot$) is to substantially reduce the flow speeds and temperatures in the outer
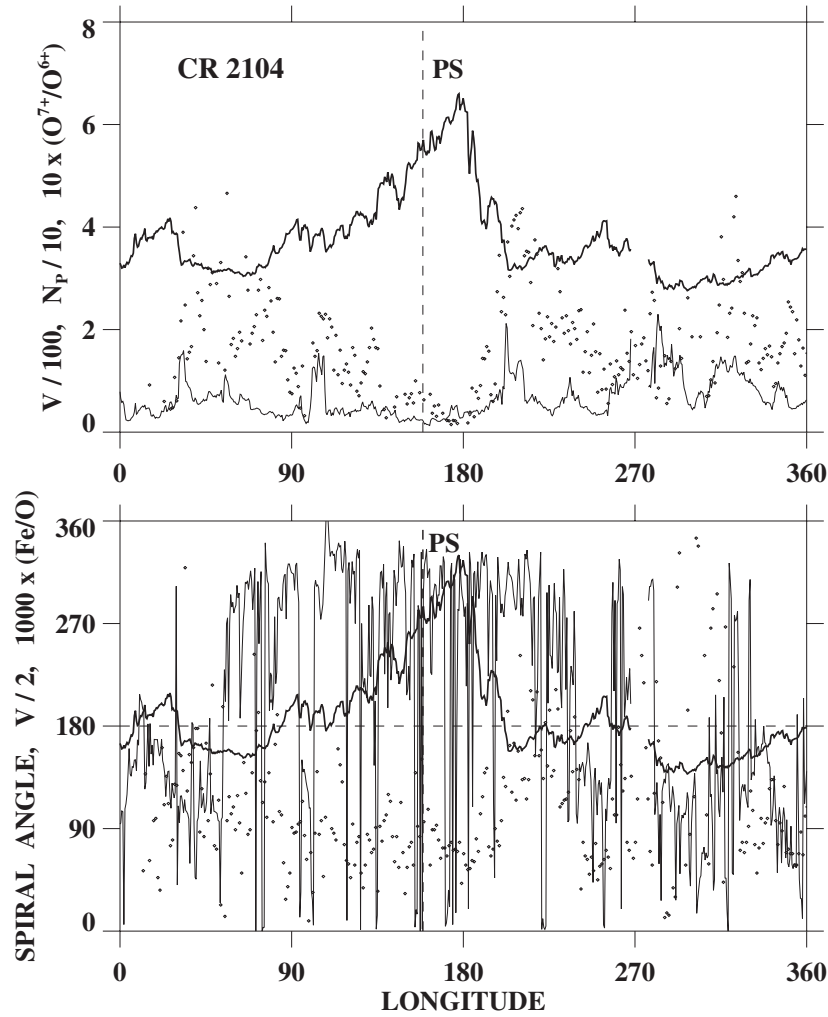
Figure 8. Solar wind measurements by *ACE* during CR 2104. Vertical dashed line marks the presumed position of the pseudostreamer; in this case, the wind from the low-latitude holes in Figure 7 have apparently merged into a single stream. Top panel: wind speed v in units of 100 km s^{-1} (thick solid line), proton density n_p in units of 10 cm^{-3} (thin solid line), and oxygen charge-state ratio (n_{O7+}/n_{O6+}) × 10 (small diamonds). Bottom panel: spiral angle in degrees (thin solid line), $v/2$ in km s^{-1} (thick solid line), and (n_{Fe}/n_O) × 1000 (small diamonds).

corona. This decrease is a consequence of the reduction in the heating rate $F_h(r)$ beyond $r \sim 1.1 \, R_\odot$ due to the continued rapid falloff of the magnetic field strength.

For comparison purposes, we have plotted two additional solutions in Figure 11, which were obtained by replacing Equation (4) by a monotonically diverging field of the form

$$B(r) = B_0 \left(\frac{R_\odot}{r} \right)^\nu \left[\frac{1 + (r/R_{ss})^{\nu-2}}{1 + (R_\odot/R_{ss})^{\nu-2}} \right], \quad (5)$$

where again $R_{ss} = 2.5 \, R_\odot$. The field strength along the flux tube thus falls off as $r^{-\nu}$ for $r \lesssim 2.5 \, R_\odot$ and as r^{-2} for $r \gg 2.5 \, R_\odot$. The dashed lines show the solution for the case $\nu = 2.83$, which gives a net expansion factor at $r = 2.5 \, R_\odot$ ($f_{ss} = 1.57$), which is the same as that for the nonmonotonically expanding case with $\nu = 7$, $R_X = 1.1 \, R_\odot$ (thick solid lines). Comparing the two solutions, we see that the monotonically diverging flux tube yields higher temperatures beyond $r \sim 1.2 \, R_\odot$ and faster outflow throughout the corona; at $r \sim 30 \, R_\odot$, $u(r)$ is ~17% higher in the monotonic case. Evidently, the reconvergence of the flux tube above the X-point in the nonmonotonic case is unable to compensate for the steep falloff of the heating rate at low heights, resulting in lower flow speeds than it would have

had if it had expanded slowly and monotonically to the same value of f_{ss}.

The dotted lines in Figure 11 show the result of setting $\nu = 4.76$ in Equation (5); this case represents a monotonically expanding flux tube having the same net expansion factor at $r = 2.5 \, R_\odot$ ($f_{ss} = 6.76$) as the nonmonotonically expanding flux tube with $\nu = 7$, $R_X = 1.5 \, R_\odot$ (thin solid lines). The solution for the monotonic flux tube yields only a slightly higher asymptotic wind speed than the corresponding solution for the nonmonotonic flux tube, with the temperature profiles being remarkably similar in the two cases. We conclude that, when the X-point is located well above the solar surface, a nonmonotonically expanding flux tube gives marginally slower wind than a monotonically expanding flux tube with the same value of f_{ss}.

These calculations suggest that the empirical v–f_{ss} relationship, based implicitly on the "normal" case of monotonic flux-tube expansion, tends to overestimate the wind speeds from pseudostreamers, particularly for small values of f_{ss}.

6. SUMMARY AND DISCUSSION

We now state our main conclusions about the nature of the solar wind from coronal pseudostreamers.
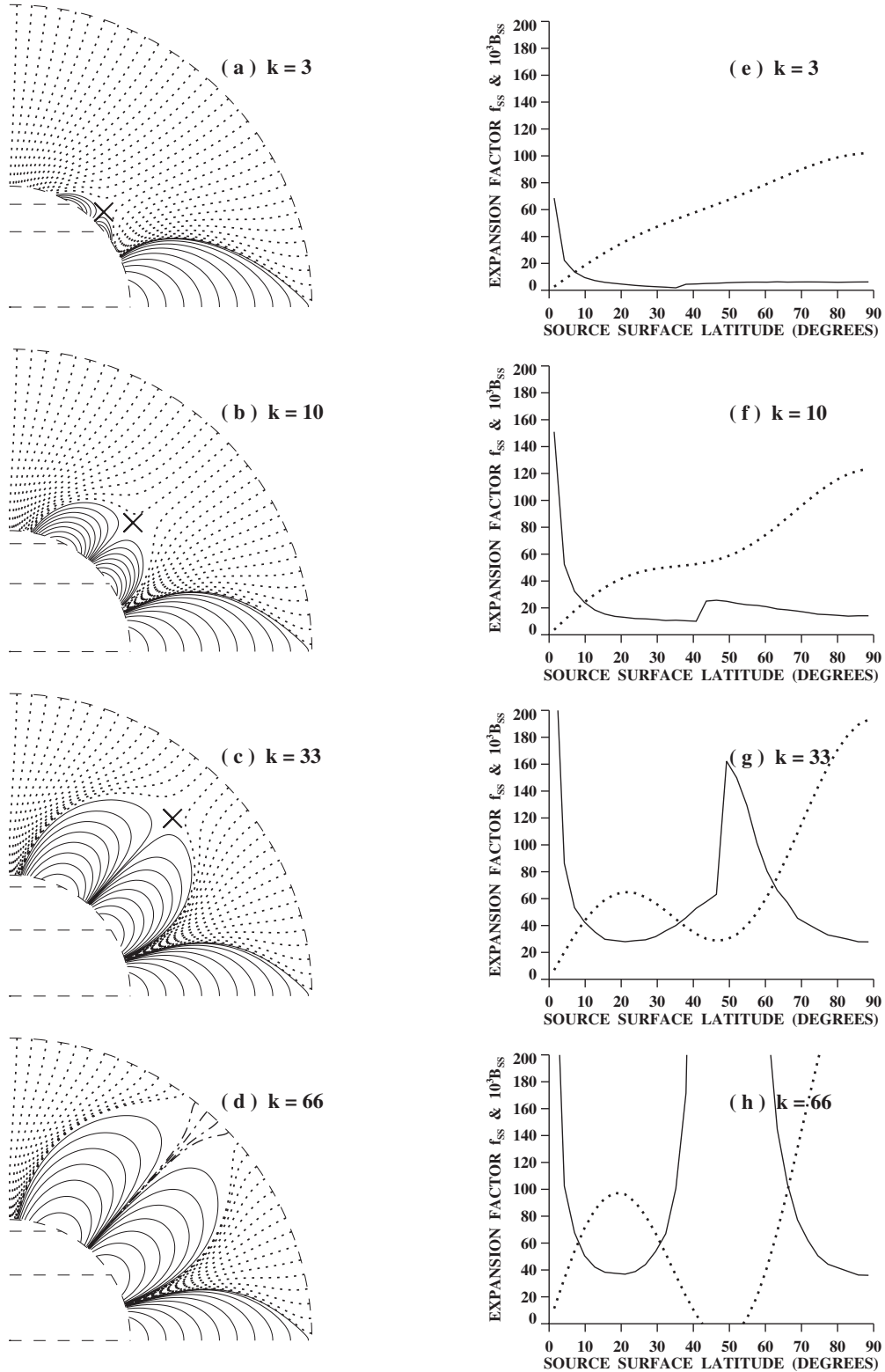
Figure 9. Idealized pseudostreamer configurations derived for an axisymmetric photospheric field of the form $B_r(R_\odot, L) = P_1(\sin L) + k P_5(\sin L)$, where L is latitude and k is an arbitrary constant. Left panels: PFSS field-line configurations for $k = 3, 10, 33,$ and 66. Horizontal dashes indicate the photospheric neutral lines, while a cross marks the X-point. Open field lines (those that reach the source surface at $r = R_{ss} = 2.5\,R_\odot$) are shown dotted if they have positive polarity, dash dotted if they have negative polarity; closed loops are solid. Right panels: variation of the source-surface expansion factor $f_{ss} = (R_\odot/R_{ss})^2(B_0/B_{ss})$ (solid lines) and source-surface field strength $|B_{ss}|$ (dotted lines) as a function of source-surface latitude, again plotted for $k = 3, 10, 33,$ and 66. (The pseudostreamer is centered on the discontinuity in f_{ss}.) As the separation between the polar and low-latitude hole (controlled by the parameter k) increases, the X-point rises and f_{ss} increases, implying lower wind speeds. For $k = 66$, the pseudostreamer splits into two helmet streamers surrounding a new hole of the opposite polarity.
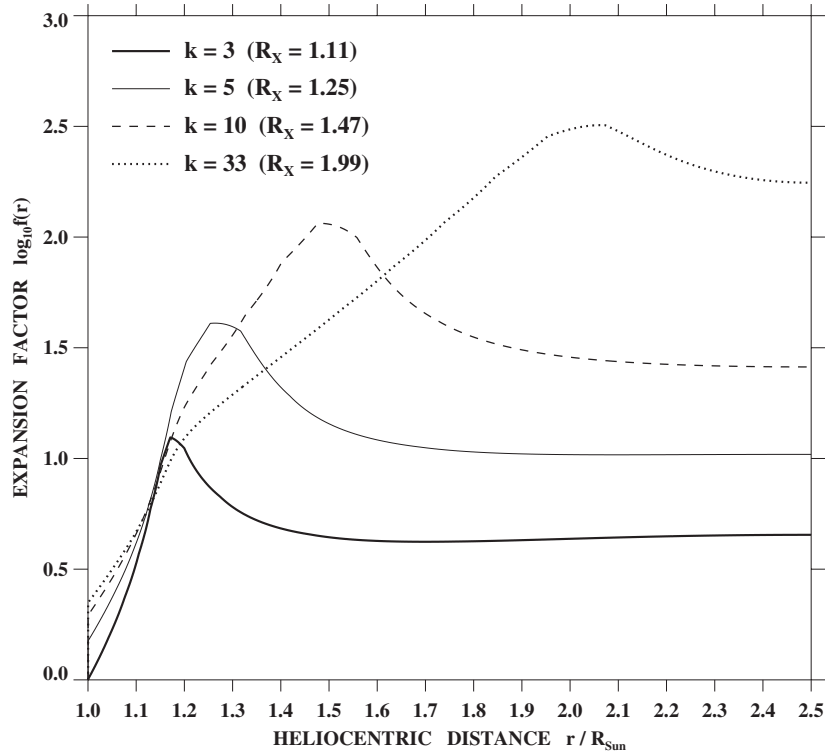
Figure 10. Variation of the expansion factor $\log_{10} f(r)$ with radial distance along an open flux tube rooted alongside the model pseudostreamer, calculated for $k = 3$ ($R_X = 1.11 R_\odot$), $k = 5$ ($R_X = 1.25 R_\odot$), $k = 10$ ($R_X = 1.47 R_\odot$), and $k = 33$ ($R_X = 1.99 R_\odot$). Here, $f(r)$ measures the net expansion of a flux tube in solid angle between the coronal base and radius r, and is proportional to the ratio of the footpoint field strength to $|B_r|$ at the given radius. In all cases, the flux tube expands rapidly between $r = R_\odot$ and $r = R_X$, attaining a maximum at $r \sim R_X$, and then falls toward a plateau where $f(r) \simeq f_{ss}$. As the X-point rises, f_{ss} increases, implying lower wind speeds according to the empirical v–f_{ss} relationship.

1. White-light coronal observations show that pseudostreamers, unlike ordinary helmet streamers, do not emit plasma blobs. The physical reason for this important but overlooked property is that the convergence of like-polarity open field lines above the pseudostreamer cusp impedes the outward expansion of the underlying coronal loops. In helmet streamers, by contrast, the field strength approaches zero at and above the cusp, and the underlying loops thus continually expand outward and pinch off to form flux ropes that are observed as streamer blobs.

2. The effect of interchange reconnection at the cusps of both pseudostreamers and helmet streamers is to inject material continually from the closed-field region into the plasma sheet, which is threaded by raylike features that presumably represent open field lines that have recently undergone such footpoint exchanges. Given the narrowness of the plasma sheet, it is unlikely that this process contributes significantly to the slow solar wind.

3. We are unable to measure unambiguously any outflows in the immediate vicinity of pseudostreamers. If such outflows exist (as we assume they do), they must be sufficiently steady and uniform as to be barely detectable in running-difference images of the white-light corona.

4. Observations of pseudostreamer crossings at 1 AU, in the form of stream–stream interfaces without polarity reversals, typically show the proton velocity dipping to a local minimum in the range $v \sim 400$–450 km s^{-1}, although speeds as low as $\sim$350 km s^{-1} (see Figure 10 in Wang et al. 2010) and as high as $\sim$550 km s^{-1} (Figure 8 above) also occur. The oxygen charge-state ratios $n_{O^{7+}}/n_{O^{6+}}$ are generally of order 0.1, larger than the values within high-speed streams but substantially lower than those in the

"classical" slow wind. The pseudostreamer wind (outside the plasma sheet itself, the properties of which we have been unable to measure here) thus has properties intermediate between fast and slow solar wind.

5. PFSS extrapolations of an idealized photospheric flux distribution show that the expansion factor f_{ss} for open field lines on either side of the pseudostreamer increases as the height of the X-point (or distance between the two like-polarity holes) increases. When $R_X \gtrsim 1.4 R_\odot$, f_{ss} has values $\gtrsim$20, corresponding to wind speeds $\lesssim$450 km s^{-1} according to the empirical v–f_{ss} relationship. Unfortunately, the cusps of pseudostreamers tend to lie below the edge of the occulting disk of spaceborne coronagraphs, making it difficult to determine the average height of the X-point from routine white-light observations. Additional factors that may contribute to the variation of the wind speeds from pseudostreamers include the areal sizes and footpoint field strengths of the underlying holes (with small active-region holes giving lower speeds) and their locations relative to the observer.

6. Open flux tubes rooted alongside pseudostreamers undergo very rapid expansion at low heights followed by reconvergence above the X-point, in contrast to the monotonic expansion undergone by most coronal-hole flux tubes. Hydrodynamic modeling, based on a coronal heating function that scales as the local magnetic field strength, confirms that the asymptotic wind speed decreases as the region of rapid expansion extends to greater heights. In addition, comparing the case of a monotonically expanding flux tube with that of a flux tube that expands nonmonotonically but has the same net expansion factor f_{ss} at the source surface, we find that the nonmonotonically expanding flux tube gives
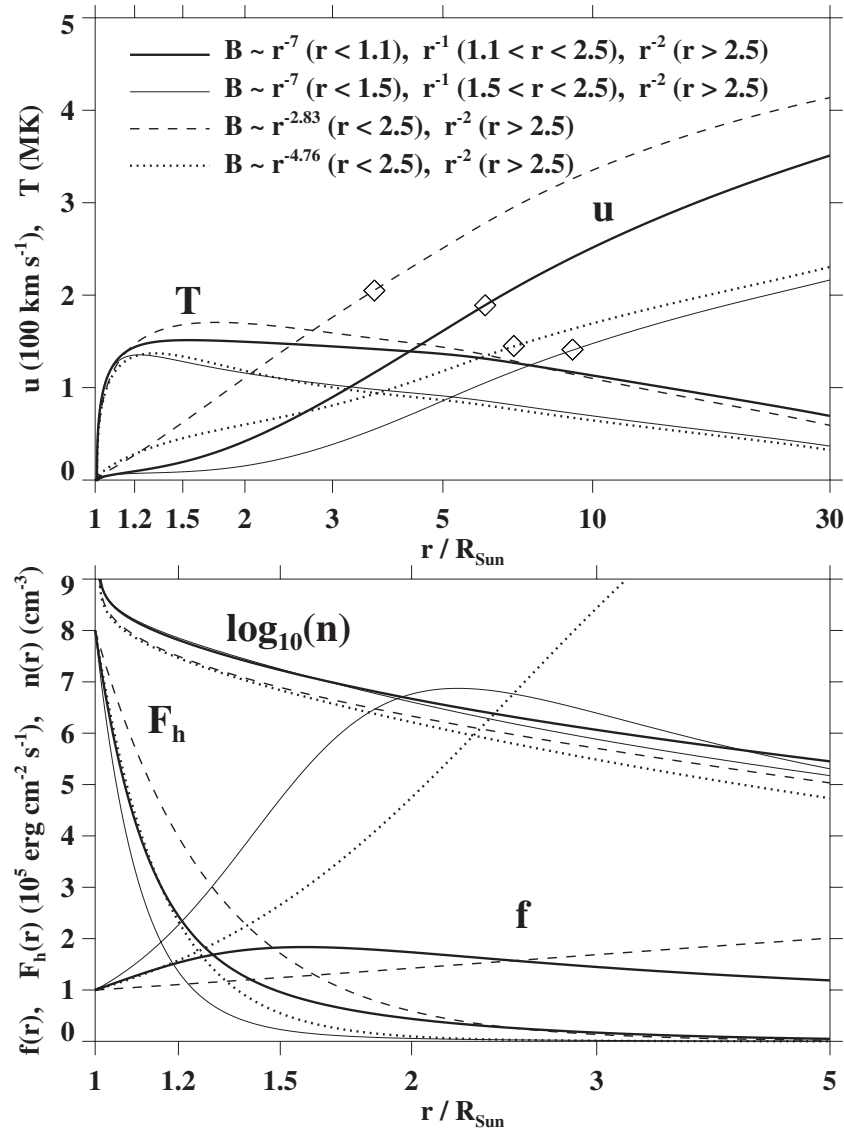
Figure 11. Four hydrodynamic wind solutions obtained by varying the radial dependence of $B(r)$ in a coronal heating function given by $F_h(r) = 8 \times 10^5$ erg cm^{-2} s^{-1} $(B/B_0)^{3/2}$. (1) $\nu = 7$, $R_X = 1.1\, R_\odot$ in Equation (4) (thick solid lines). (2) $\nu = 7$, $R_X = 1.5\, R_\odot$ in Equation (4) (thin solid lines). (3) $\nu = 2.83$ in Equation (5) (dashed lines). (4) $\nu = 4.76$ in Equation (5) (dotted lines). The third (fourth) solution is for a monotonically expanding flux tube having the same net expansion at $r = R_{ss} = 2.5\, R_\odot$ as the first (second) solution. Top panel: flow speed $u(r)$ in units of 100 km s^{-1} and temperature $T(r)$ in MK, plotted between $r = R_\odot$ and $r = 30\, R_\odot$. Diamonds mark the sonic point. Bottom panel: proton density $\log_{10}[n(r)/\text{cm}^{-3}]$, mechanical energy flux density $F_h(r)/(10^5$ erg cm^{-2} s$^{-1})$, and expansion factor $f(r)$ between $r = R_\odot$ and r, plotted out to $r = 5\, R_\odot$.

significantly lower wind speeds when R_X is located at low heights. These computations suggest that the empirical v–f_{ss} relationship, which is based on statistical averages dominated by monotonically expanding flux tubes, significantly overestimates the wind speeds from pseudostreamers when f_{ss} is small.

An important implication of this study is that pseudostreamers and their immediate surroundings are unlikely to be a major source of the slow solar wind. Rather than being characterized by high temporal variability, white-light observations show pseudostreamers to be remarkably quiescent compared with helmet streamers. In situ measurements at pseudostreamer crossings suggest that their compositional properties, as well as their proton speeds, lie somewhere between those of fast and slow solar wind.

More generally, this study provides further evidence that interchange reconnection does not give rise to the bulk of the

low-speed solar wind, although it is likely to be the mechanism that supplies material to helmet-streamer and pseudostreamer plasma sheets and to the ubiquitous plumes that overlie small bipoles inside coronal holes. In the S-web model of Antiochos et al. (2011), an implicit assumption is that all streamers, including pseudostreamers, continually emit bloblike ejecta, which clearly do provide some contribution to the slow solar wind and its temporal variability (Wang et al. 2000; Kilpua et al. 2009; Song et al. 2009; Rouillard et al. 2010a, 2010b). It is then argued that, because the network of separatrices (dominated by pseudostreamers) forms a wide band surrounding the HCS, most of the observed low-speed wind, which extends to at least ∼15° on each side of the HCS near sunspot minimum, can be accounted for by this type of transient outflow from closed-field regions. As we have emphasized here and in Wang et al. (2007b), however, pseudostreamers do not produce plasma blobs, even though they undergo continual interchange reconnection at their cusps. The same holds for

coronal plumes ("mini-pseudostreamers"), which are likewise remarkably quiescent and which have been notoriously difficult to identify in the in situ solar wind (see Wilhelm et al. 2011; Velli et al. 2011). Indeed, because the X-point of a plume is located very near the solar surface, the calculations of Sections 4 and 5 suggest that plumes should give rise to moderately fast rather than slow wind; mixing with the even faster interplume component via shear flow instabilities would then act to smear out any distinctive plume signatures at 1 AU.

As we have again seen in this study, the flux-tube expansion factor f_{ss} alone does not capture all of the effects involved in heating and accelerating the solar wind. In Section 5, we found that monotonically and nonmonotonically expanding flux tubes having the same value of f_{ss} can give rise to different wind speeds. In particular, the empirical v–f_{ss} relationship overestimates the wind speed from pseudostreamers, where the rapid expansion of the flux tube at low heights leads to a steep falloff in the coronal heating rate that is not offset by the subsequent reconvergence of the flux tube; the wind thus ends up slower than for the corresponding case of monotonic expansion all the way to the source surface. This effect is particularly significant for small values of f_{ss}, but less so for large values, when the X-point is located well above the coronal base. In principle, it may be possible to improve the wind-speed prediction algorithm by employing $f(r)$ in place of f_{ss} to characterize the flux-tube expansion rate in the corona.

REFERENCES

Antiochos, S. K., Mikić, Z., Titov, V. S., Lionello, R., & Linker, J. A. 2011, ApJ, 731, 112
Arge, C. N., & Pizzo, V. J. 2000, J. Geophys. Res., 105, 10465
Borrini, G., Gosling, J. T., Bame, S. J., Feldman, W. C., & Wilcox, J. M. 1981, J. Geophys. Res., 86, 4565
Chen, Y., Li, X., Song, H. Q., et al. 2009, ApJ, 691, 1936
Cranmer, S. R. 2009, Living Rev. Sol. Phys., 6, 3
Crooker, N. U., Gosling, J. T., & Kahler, S. W. 2002, J. Geophys. Res., 107, 1028
Crooker, N. U., Huang, C.-L., Lamassa, S. M., et al. 2004, J. Geophys. Res., 109, A03107
Crooker, N. U., & Owens, M. J. 2011, Space Sci. Rev., doi:10.1007/s11214-011-9748-1
Edmondson, J. K. 2011, Space Sci. Rev., doi:10.1007/s11214-011-9767-y
Einaudi, G., Chibbaro, S., Dahlburg, R. B., & Velli, M. 2001, ApJ, 547, 1167
Endeve, E., Holzer, T. E., & Leer, E. 2004, ApJ, 603, 307
Eselevich, V. G., Fainshtein, V. G., & Rudenko, G. V. 1999, Sol. Phys., 188, 277
Feldman, U., Landi, E., & Schwadron, N. A. 2005, J. Geophys. Res., 110, A07109
Fisk, L. A., Zurbuchen, T. H., & Schwadron, N. A. 1999, ApJ, 521, 868
Geiss, J., Gloeckler, G., von Steiger, R., et al. 1995, Science, 268, 1033
Gosling, J. T., Birn, J., & Hesse, M. 1995, Geophys. Res. Lett., 22, 869
Grappin, R., Cavillier, E., & Velli, M. 1997, A&A, 322, 659
Jones, S. I., & Davila, J. M. 2009, ApJ, 701, 1906
Kahler, S., Jibben, P., & DeLuca, E. E. 2010, Sol. Phys., 262, 135
Kilpua, E. K. J., Luhmann, J. G., Gosling, J., et al. 2009, Sol. Phys., 256, 327
Krista, L. D., Gallagher, P. T., & Bloomfield, D. S. 2011, ApJ, 731, L26
Leer, E., & Holzer, T. E. 1980, J. Geophys. Res., 85, 4681
Liewer, P. C., Neugebauer, M., & Zurbuchen, T. 2004, Sol. Phys., 223, 209
Linker, J. A., Lionello, R., Mikić, Z., Titov, V. S., & Antiochos, S. K. 2011, ApJ, 731, 110
Lionello, R., Linker, J. A., & Mikić, Z. 2009, ApJ, 690, 902
Lionello, R., Riley, P., Linker, J. A., & Mikić, Z. 2005, ApJ, 625, 463
Liu, Y. 2007, ApJ, 654, L171
Liu, Y., & Hayashi, K. 2006, ApJ, 640, 1135
Luhmann, J. G., Lee, C. O., Li, Y., et al. 2009, Sol. Phys., 256, 285
Morgan, H. 2011, ApJ, 738, 190
Morgan, H., & Habbal, S. R. 2010, ApJ, 710, 1
Nash, A. G., Sheeley, N. R., Jr., & Wang, Y.-M. 1988, Sol. Phys., 117, 359
Neugebauer, M., Liewer, P. C., Goldstein, B. E., Zhou, X., & Steinberg, J. T. 2004, J. Geophys. Res., 109, A10102
Neugebauer, M., Liewer, P. C., Smith, E. J., Skoug, R. M., & Zurbuchen, T. H. 2002, J. Geophys. Res., 107, 1488
Owens, M. J., & Crooker, N. U. 2006, J. Geophys. Res., 111, A10104
Pasachoff, J. M., Rušin, V., Druckmüllerová, H., et al. 2011, ApJ, 734, 114
Pinto, R., Grappin, R., Wang, Y.-M., & Léorat, J. 2009, A&A, 497, 537
Poduval, B., & Zhao, X. P. 2004, J. Geophys. Res., 109, A08102
Raju, K. P., Bromage, B. J. I., Chapman, S. A., & Del Zanna, G. 2005, A&A, 432, 341
Riley, P., Lionello, R., Linker, J. A., et al. 2011, Sol. Phys., 274, 361
Riley, P., Mikic, Z., Lionello, R., et al. 2010, J. Geophys. Res., 115, A06104
Rouillard, A. P., Davies, J. A., Lavraud, B., et al. 2010a, J. Geophys. Res., 115, A04103
Rouillard, A. P., Lavraud, B., Davies, J. A., et al. 2010b, J. Geophys. Res., 115, A04104
Rouillard, A. P., Sheeley, N. R., Jr., Cooper, T. J., et al. 2011, ApJ, 734, 7
Schwadron, N. A., Connick, D. E., & Smith, C. 2010, ApJ, 722, L132
Schwadron, N. A., Fisk, L. A., & Zurbuchen, T. H. 1999, ApJ, 521, 859
Sheeley, N. R., Jr., Lee, D. D.-H., Casto, K. P., Wang, Y.-M., & Rich, N. B. 2009, ApJ, 694, 1471
Sheeley, N. R., Jr., & Wang, Y.-M. 1991, Sol. Phys., 131, 165
Sheeley, N. R., Jr., Wang, Y.-M., Hawley, S. H., et al. 1997, ApJ, 484, 472
Song, H. Q., Chen, Y., Liu, K., Feng, S. W., & Xia, L. D. 2009, Sol. Phys., 258, 129
Suess, S. T., Wang, A.-H., & Wu, S. T. 1996, J. Geophys. Res., 101, 19957
Titov, V. S., Mikić, Z., Linker, J. A., Lionello, R., & Antiochos, S. K. 2011, ApJ, 731, 111
Velli, M., Lionello, R., Linker, J. A., & Mikić, Z. 2011, ApJ, 736, 32
von Steiger, R., Schwadron, N. A., Fisk, L. A., et al. 2000, J. Geophys. Res., 105, 27217
Wang, Y.-M., Biersteker, J. B., Sheeley, N. R., Jr., et al. 2007a, ApJ, 660, 882
Wang, Y.-M., Hawley, S. H., & Sheeley, N. R., Jr. 1996, Science, 271, 464
Wang, Y.-M., Ko, Y.-K., & Grappin, R. 2009, ApJ, 691, 760
Wang, Y.-M., & Muglach, K. 2008, Sol. Phys., 249, 17
Wang, Y.-M., Nash, A. G., & Sheeley, N. R., Jr. 1989, Science, 245, 712
Wang, Y.-M., Robbrecht, E., Rouillard, A. P., Sheeley, N. R., Jr., & Thernisien, A. F. R. 2010, ApJ, 715, 39
Wang, Y.-M., & Sheeley, N. R., Jr. 1990, ApJ, 355, 726
Wang, Y.-M., & Sheeley, N. R., Jr. 1993, ApJ, 414, 916
Wang, Y.-M., & Sheeley, N. R., Jr. 2004, ApJ, 612, 1196
Wang, Y.-M., Sheeley, N. R., Jr., & Rich, N. B. 2007b, ApJ, 658, 1340
Wang, Y.-M., Sheeley, N. R., Jr., Socker, D. G., Howard, R. A., & Rich, N. B. 2000, J. Geophys. Res., 105, 25133
Wang, Y.-M., Sheeley, N. R., Jr., Walters, J. H., et al. 1998, ApJ, 498, L165
Wilhelm, K., Abbo, L., Auchère, F., et al. 2011, A&AR, 19, 35
Yang, L., Feng, X., Xiang, C., Zhang, S., & Wu, S. T. 2011, Sol. Phys., 271, 91
Zhao, L., Zurbuchen, T. H., & Fisk, L. A. 2009, Geophys. Res. Lett., 36, L14104
Zhao, X. P., & Webb, D. F. 2003, J. Geophys. Res., 108, 1234